

Axisymmetric gas–liquid displacement flow under a confined elastic slabGunnar G. Peng ^{1,2} Callum Cuttle ³ Christopher W. MacMinn ³ and Draga Pihler-Puzović ¹¹*Department of Physics & Astronomy and Manchester Centre for Nonlinear Dynamics,
University of Manchester, Oxford Road, M13 9PL Manchester, United Kingdom*²*Department of Mathematics, Imperial College London, London SW7 2AZ, United Kingdom*³*Department of Engineering Science, University of Oxford, Parks Road, Oxford OX1 3PJ, United Kingdom*

(Received 14 December 2022; accepted 25 August 2023; published 21 September 2023)

A circular Hele-Shaw cell bounded by a volumetrically confined elastic solid can act as a fluidic fuse: during radially outward fluid flow, the solid deforms in response to the viscous pressure field such that the gap expands near the inlet (at the center) and contracts near the outlet (around the rim). If the flow rate exceeds a critical value, then the gap at the outlet can close completely, interrupting/choking the flow. Here, we consider the injection of gas into such a soft-walled Hele-Shaw cell filled with viscous liquid. Our theoretical model and numerical simulations for axisymmetric flow driven by the injection of an expanding gas bubble show that the bubble increases the critical flow rate of choking via two mechanisms. First, as the interface approaches the rim, it reduces the length over which the viscous pressure gradient deforms the solid, which increases the critical flow rate above which choking occurs. Second, compression of the gas reduces the outlet flow rate relative to the inlet flow rate. As a consequence, for large injection rates, a near-choking regime is established in which the outlet flow rate becomes independent of the injection rate and instead depends only on the instantaneous position of the interface. Our traveling-wave model for the advancement of the bubble front will enable future reduced-order modeling of nonaxisymmetric problems, such as viscous fingering.

DOI: [10.1103/PhysRevFluids.8.094005](https://doi.org/10.1103/PhysRevFluids.8.094005)**I. INTRODUCTION**

The interaction of two-phase viscous flows with soft deformable components is common to many natural and industrial settings, including flow in soft porous media [1], in passive microfluidic devices [2], and in biological systems. For example, in the pulmonary airway tree under pathological conditions, air entering the compliant lungs encounters plugs of mucus that occlude its passageways [3]. Other types of low-Reynolds-number fluid-structure interaction (low-Re FSI) have recently been exploited for technological progress, for example, in improving the manufacturing quality of products [4], personalizing diagnostic tools [5], and developing soft robotics [6]. Fundamental understanding of such complex flows can be gained by studying much simpler model problems.

Low-Re FSI is common in microfluidics, where the small length scales and PDMS-based flow cells naturally yield interactions between viscous flows and soft boundaries [7]. Moreover, microfluidic devices often have a Hele-Shaw geometry and may contain even softer components for functional reasons [8]. Many microfluidic analogs of electronic components, which passively regulate flow without external hardware, have previously been introduced. They include fluidic valves

Published by the American Physical Society under the terms of the [Creative Commons Attribution 4.0 International](https://creativecommons.org/licenses/by/4.0/) license. Further distribution of this work must maintain attribution to the author(s) and the published article's title, journal citation, and DOI.

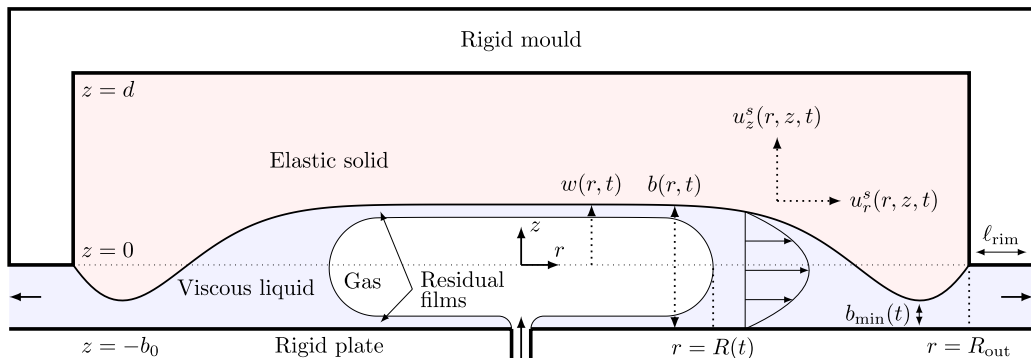


FIG. 1. Schematic of radially outward gas–liquid displacement in a Hele-Shaw cell bounded by a confined elastic solid.

[9,10], capacitors [11], and diodes [12], as well as soft fuselike devices [13], in which a portion of the wall is replaced by an elastic arc that can snap from one configuration to another, thereby constricting the channel. However, instead of completely interrupting the flow, this particular device relies on redirecting the fluid to another rigid channel, so that the soft component acts more like a current-dependent switch. In the majority of microfluidic devices that involve fluid-structure interactions, flow interacts with thin membranes or slender bodies. Even when interactions with thick slabs of elastic material were explored in microfluidics, e.g., by Ref. [14], the wall was not volumetrically confined, leaving the flow channel free to expand arbitrarily as fluid is injected. By contrast, many natural systems, such as brain tissue and cerebrospinal fluid in the cranium [15], are subject to volumetric confinement, which can generate novel fluid-structure interaction (FSI) phenomena yet to be exploited in engineering applications. Hence, practical understanding of confined microfluidic components is relatively underdeveloped.

Here, we study gas–liquid displacement in a volumetrically confined soft Hele-Shaw cell (soft cell), as shown schematically in Fig. 1. The soft cell is an established testbed for studying low-Re FSI. For single-phase flows, the system exhibits a critical “choking” behavior [16]: viscous pressure gradients deform the soft plate, squeezing material from the inlet toward the outlet, where it accumulates and bulges into the flow path. Beyond a critical injection rate, the outlet is occluded entirely, preventing flow through the cell. Hence, the response of the soft cell is directly analogous to that of a fuse. The choking effect is unique to volumetrically confined systems. In contrast, in a Hele-Shaw cell in which one wall is replaced by a thin, unconfined elastic membrane, deformation can occur via expansion, and the flow path remains unobstructed [17–19]. Other examples of confined systems that display choking behavior are the single-phase flow of liquid through a column of deformable hydrogel beads [20], and the two-phase gas-driven displacement of a mixture of aqueous liquid and hydrophilic solid grains in a capillary tube [21]; in both of these examples, the displaced grains compact to form an impermeable layer that obstructs the flow. Here, we examine two-phase displacement flows in the soft Hele-Shaw cell and their impact on the choking phenomenon.

Building on the single-phase study of Box *et al.* [16], Peng *et al.* [22] examined gas injection into liquid-filled soft cells, revealing a host of complexities arising from the displacement flow. Their work focused on the viscous-fingering instability, which has been extensively studied in rigid Hele-Shaw cells. At low flow rates, the interface between the two fluids is always circular (i.e., stable). However, if a less viscous fluid (e.g., air) displaces a more viscous fluid (e.g., glycerol) at a sufficiently high rate, then the interface becomes unstable and develops distinct fingers that subsequently compete, split, and branch, forming a complex interfacial pattern [23]. This fingering instability can be suppressed to higher flow rates if one of the walls of the Hele-Shaw cell is replaced by a thin, unconfined elastic membrane, which allows the injected volume to be accommodated in large part by inflation rather than viscous displacement [24,25]. Interestingly, the deformation of the

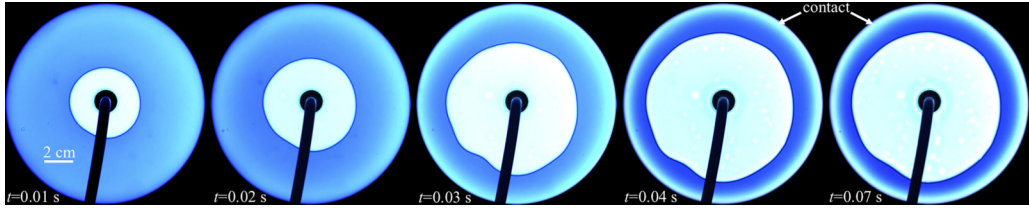


FIG. 2. Top view images from preliminary experiments with an approximately circular interface at various times t from the start of the experiment. The injected gas bubble displaces glycerol (dye blue) in the narrow gap of a soft Hele-Shaw cell. Flow-induced deformation of the elastomer eventually leads to contact between the soft slab and the glass plate in the vicinity of the cell rim (visible as a white band encircling the cell), trapping the interface within the cell. The experimental parameters are: cell radius $R_{\text{out}} = 60$ mm and initial gap $b_0 = 2$ mm; elastomer thickness $d = 15$ mm, shear modulus $G = 1.36$ kPa and Poisson's ratio $\nu = 0.495$; liquid viscosity $\mu = 0.72$ Pa s and surface tension $\gamma = 63$ mN/m; imposed flow rate $Q_0 = 450$ ml/min.

flow cell remains roughly axisymmetric and independent of the morphology of the displacement front [26], unless the elastic membrane is very compliant [27]. By contrast, ramified interfacial structures (fingers) reminiscent of those observed in rigid cells develop in the confined soft cell, where deformations are far less pronounced but may be strongly localized around individual air fingers. Comparison between experiments with fingering and an axisymmetric model revealed a subtle interplay between viscous fingering and FSI in the soft cell that can either promote or suppress choking, depending on finger morphology [22]. However, choking is also observed in experiments where the interface remains approximately circular (Fig. 2). Here, choking is modified by more fundamental aspects of the two-phase flow: namely, displacement of the viscous phase and compression of the injected gas. These features were identified by Peng *et al.* [22] but were not systematically studied.

For gas-driven flows, further complexity arises from the compression of the injected gas, which may be significant at the typical viscous pressure variations of the displacement flow (i.e., a significant fraction of atmospheric pressure; Peng *et al.* [22] measured gas gauge pressures up to 0.4 bar). In a typical displacement flow, the viscosity of the gas is negligible compared to that of the displaced liquid, meaning changes in the density of the gas (i.e., compression) are spatially uniform but coupled in time to the evolving driving pressure. This is distinct from compressible gas flow in very long microchannels or microtubes, where the viscous stresses in the gas itself lead to spatial variations in density [28,29]. In existing literature, gas compression is often neglected or carefully avoided, e.g., by extracting liquid rather than injecting gas [30]. However, compression is unavoidable in many practical settings, such as during the gas-driven displacement of granular suspensions [31], during gas invasion into liquid-saturated porous media [32], during foam-driven hydraulic fracturing [33], or in soft microfluidics carrying a viscous flow with a small amount of air trapped in the system [34]. Fundamentally, gas compression produces unsteady flow rates, distinct from the nominally constant injection rate set by a syringe pump, which are directly coupled to the displacement flow. These unsteady dynamics can result in the sharp transition from quasisteady to burstlike displacements in capillary tubes [35], delayed onset of the viscous fingering instability in rigid Hele-Shaw cells [36], and stick-slip choking dynamics [37] and complex pattern formation [31] in the gas-driven displacement of frictional granular suspensions in Hele-Shaw cells.

Even in the absence of viscous fingering and compression, displacement flows in deformable geometries are inherently unsteady due to the time-evolution of viscous pressures as the interface between the phases advances. In a soft cell, displacement of liquid by an inviscid gas reduces the length of the region squeezed toward the outlet by viscous pressure gradients, a key mechanism by which choking is suppressed [22]. In the soft Hele-Shaw cell, the evolution of viscous stresses and, hence, the time-dependent injection rate are directly coupled to the FSI-mediated deformation of the soft plate. We depart from the previous study of Peng *et al.* [22] and focus on the roles of gas

compression and viscous pressure gradients on choking in an axisymmetric geometry by exploring a mathematical model of an axisymmetric two-phase lubrication flow under a confined elastic slab. Thus, we decouple the influence of the two-phase displacement from that of the viscous fingering in experiments by Peng *et al.* [22].

This paper is laid out as follows. We present the axisymmetric governing equations and nondimensionalization in Sec. II, followed by a description of the gas–liquid displacement flow at low injection rates in Sec. III. For higher flow rates, we study the impact of gas–liquid displacement on choking in Sec. IV, by relating the deformation of the elastomer to the proximity of the bubble to the cell rim (Sec. IV A) and identifying a near-choking regime when the compression of the gas is significant (Sec. IV B). We investigate the dynamics of the advancing bubble front in Sec. V. We summarize and discuss the results in Sec. VI.

II. THEORETICAL MODEL

We adapt the model and numerical simulations presented and validated by Ref. [22] to account for compression of the injected gas, in the form of a nonlinear coupling between the rate of change of air volume in the cell and the air pressure in the cell.

A. Governing equations

The setup is shown in Fig. 1. We consider a Hele-Shaw cell of initial (relaxed) gap thickness b_0 , bounded by a rigid wall below and by an elastic slab above. The elastic slab is a cylinder of radius R_{out} , thickness $d \lesssim R_{\text{out}}$, and shear modulus G that is confined both around the outer rim and from above within a rigid mould. The cell is initially filled with liquid of viscosity μ . A gas bubble is injected at the nominal volumetric flow rate Q_0 at the center of the cell, displacing the liquid and also deforming the elastomer. We neglect inertia and gravity, as well as the compressibility of the solid and of the liquid.

We employ cylindrical polar coordinates (r, θ, z) with the surface of the undeformed elastic solid located at $z = 0$, and the center of the cell at $r = 0$. We assume axisymmetry, as discussed above, so that there is no explicit dependence on the azimuthal angle θ .

One key assumption in our analysis is that the initial cell gap b_0 and the vertical deformation w are small compared with the initial slab thickness d , i.e., that $b_0, w \ll d$. As a result, the gap thickness can change significantly from its initial value, while the strains in the elastic solid remain small, allowing us to adopt linear elasticity. For a deformation characterized by displacement \mathbf{u}^s , stress tensor σ^s , and pressure $p^s = -(\text{Tr } \sigma^s)/3$, the equations for linear elasticity, incompressibility, and mechanical equilibrium in the solid take the form

$$\sigma^s = -p^s \mathbf{I} + G[\nabla \mathbf{u}^s + (\nabla \mathbf{u}^s)^T], \quad \nabla \cdot \mathbf{u}^s = 0, \quad (1a)$$

$$\mathbf{0} = \nabla \cdot \sigma^s = -\nabla p^s + G\nabla^2 \mathbf{u}^s, \quad (1b)$$

in the solid domain $0 \leq r \leq R_{\text{out}}, 0 \leq z \leq d$. Here, Tr denotes the trace, $\nabla = \mathbf{e}_r \partial_r + \mathbf{e}_\theta (1/r) \partial_\theta + \mathbf{e}_z \partial_z$ is the gradient operator with $\mathbf{e}_r, \mathbf{e}_\theta$, and \mathbf{e}_z the coordinate unit vectors, \mathbf{I} is the identity tensor, and superscript T denotes transpose. We impose that the solid is adhered to the mould and that there is no singularity at the center,

$$\mathbf{u}^s = \mathbf{0} \quad \text{at } r = R_{\text{out}} \text{ and at } z = d, \quad u_r^s = \partial_r u_z^s = 0 \quad \text{at } r = 0. \quad (2)$$

The solid is coupled to the flow in the gap via the vertical displacement $w(r, t)$ of the surface and the gauge pressure $p(r, t)$ on the surface (measured relative to atmospheric pressure), while the viscous shear stress from the flow on the surface can be neglected due to the assumption that $b_0, w \ll d$,

$$u_z^s|_{z=0} = w, \quad \sigma_{zz}^s|_{z=0} = -p, \quad \sigma_{rz}^s|_{z=0} = 0. \quad (3)$$

The local gap $b(r, t)$ is related to the vertical deformation $w(r, t)$ of the solid surface by

$$b(r, t) = b_0 + w(r, t). \quad (4)$$

For the flow, we split the domain into two parts. In the bubble region $r < R(t)$, the pressure is spatially uniform:

$$p(r, t) = p_b(t) \quad \text{in } r < R(t). \quad (5)$$

In the liquid region $r > R(t)$, we adopt the standard Hele-Shaw assumption that the pressure is vertically uniform and equal to $p(r, t)$ to leading order in b_0/R_{out} , satisfying the lubrication equation

$$\dot{b} = \nabla_H \cdot \left(\frac{b^3}{12\mu} \nabla_H p \right) \quad \text{in } r > R(t). \quad (6)$$

Here, the over-dot is the partial derivative with respect to time and $\nabla_H = \mathbf{e}_r \partial_r + \mathbf{e}_\theta (1/r) \partial_\theta$ is the horizontal gradient operator. (Note that we neglect any horizontal velocity from the solid onto the fluid, due to $b_0 \ll d$.) We do not model the advancing gas–liquid interface at the displacement front $r = R(t)$ in detail. Instead, following Peng *et al.* [38], we employ approximate kinematic and dynamic boundary conditions appropriate for a growing bubble in a Hele-Shaw cell with rigid and parallel walls,

$$(1 - f_1) \dot{R} = -\frac{b^2}{12\mu} \frac{\partial p}{\partial r}, \quad p - p_b = -\frac{2\gamma}{b} (1 + f_2) - \frac{\pi \gamma}{4 R} \quad \text{at } r = R^+. \quad (7a)$$

These conditions depend on the instantaneous capillary number $\text{Ca} = \mu \dot{R} / \gamma$ via two fitting functions,

$$f_1(\text{Ca}) = \frac{\text{Ca}^{2/3}}{0.76 + 2.16 \text{Ca}^{2/3}}, \quad f_2(\text{Ca}) = \frac{\text{Ca}^{2/3}}{0.26 + 1.48 \text{Ca}^{2/3}} + 1.59 \text{Ca}, \quad (7b)$$

which, respectively, describe the thickness of the residual liquid films on the cell walls behind the front and the additional pressure drop due to viscous resistance near the front.

Initially, the cell is undeformed and contains a small bubble of radius R_{init} (which we take to be $R_{\text{init}} = d/2$ unless otherwise specified),

$$w|_{t=0} = 0, \quad R|_{t=0} = R_{\text{init}}. \quad (8)$$

At the cell outlet $r = R_{\text{out}}$, we impose atmospheric pressure (i.e., zero gauge pressure) and let $Q(t)$ denote the flow rate of liquid leaving the cell,

$$p|_{r=R_{\text{out}}} = 0, \quad Q(t) = -2\pi R_{\text{out}} \left. \frac{b^3}{12\mu} \frac{\partial p}{\partial r} \right|_{r=R_{\text{out}}}. \quad (9)$$

Here, we have neglected the contribution to the viscous pressure drop from the thickness ℓ_{rim} of the rim of the mould: Past the edge of the elastic solid, the rim creates a region of constant cell gap $b = b_0$, which could be accounted for by solving the lubrication equation (6) with the given flow rate $Q(t)$, resulting in the alternative pressure condition $p = (Q/2\pi) \ln(1 + \ell_{\text{rim}}/R_{\text{out}})$ at $r = R_{\text{out}}$, but we neglect this effect as $\ell_{\text{rim}}/R_{\text{out}} \ll 1$, and use Eq. (9) instead.

B. Gas injection models

Due to incompressibility of the liquid and solid, the outlet flow rate $Q(t)$ is also the rate of change of gas volume in the cell. We assume in all cases that gas is injected at a constant nominal flow rate Q_0 . If the compression of the gas is negligible, then we simply have

$$Q(t) = Q_0. \quad (10)$$

However, the elevated pressure $p_b(t)$ in the bubble compresses the gas, which may lead to a significant deviation between $Q(t)$ and Q_0 . We assume that the heat generated by compression is

rapidly lost to the environment, so that the gas can be approximated as isothermal. If the mass of gas in the system has volume $V_u(t)$ under atmospheric pressure p_a , then, after compression to an absolute pressure $p_a + p_b(t)$ its volume is $V_b = V_u/(1 + p_b/p_a)$. The compression of the injected gas proceeds differently depending on the method of its injection, and we consider two different methods that have been used in experiments [22]. For injection using a syringe pump at a nominal rate Q_0 , the pump chamber, tubing and bubble together form a sealed mass of gas with original volume $V_u = V_{\text{init}}$, so the flow rate is

$$Q(t) = Q_0 + \dot{V}_b = Q_0 + \frac{d}{dt} \left[\frac{V_{\text{init}}}{(1 + p_b(t)/p_a)} \right] \quad (\text{syringe pump}). \quad (11a)$$

For injection from a pressurized gas bottle with pressure $\gg p_a$ via a needle resistor tuned to result in a fixed volume flow rate Q_0 of atmospheric-pressure gas downstream, the total uncompressed volume of air in the system increases as $V_u = V_{\text{init}} + Q_0 t$, where V_{init} is the initial volume of air in the cell and the tubing downstream of the resistor, so the flow rate is

$$Q(t) = \dot{V}_b = \frac{d}{dt} \left[\frac{V_{\text{init}} + Q_0 t}{(1 + p_b(t)/p_a)} \right] \quad (\text{pressurized bottle}). \quad (11b)$$

Although the two expressions (11) are similar, and approximately equal when V_{init} is sufficiently large [35], an important difference between the two injection methods is how small V_{init} could reasonably be in practice. For injection using a syringe pump, the initial gas volume must be at least as large as the volume of the flow cell, to allow the injection to proceed until the bubble reaches the rim of the cell. For injection using a pressurized bottle, however, the initial gas volume can be much lower, just equal to the volume of the initial bubble in the cell, assuming that the tubing volume can be neglected. As we do not seek to investigate the effects of varying V_{init} in detail, we simply choose to use

$$V_{\text{init}} = \pi b_0 R_{\text{out}}^2 \quad (\text{syringe pump}), \quad V_{\text{init}} = \pi b_0 R_{\text{init}}^2 \quad (\text{pressurized bottle}), \quad (12)$$

which are representative of typical experimental conditions for each injection method. We note that the difference in results between the two cases is due to both the difference between the methods (11) and the different choices of initial gas volume (12). The role of these differences and their effect on the two-phase displacement in a rigid cell are investigated in detail in Cuttle *et al.* [36].

C. Nondimensionalization

We nondimensionalize the governing equations by scaling lengths with the solid thickness d , scaling deflections with the initial gap b_0 , and seeking a balance between all terms in the lubrication equation (6). Thus, the nondimensional quantities are given by

$$\begin{aligned} (\mathbf{x}^*, R^*) &= \frac{(\mathbf{x}, R)}{d}, & (\mathbf{u}^{s*}, w^*, b^*) &= \frac{(\mathbf{u}^s, w, b)}{b_0}, & (p^*, p_b^*, p^{s*}, \sigma^{s*}) &= \frac{(p, p_b, p^s, \sigma^s)}{Gb_0/d}, \\ t^* &= \frac{t}{12\mu d^3/(Gb_0^3)}, & Q^* &= \frac{Q}{2\pi Gb_0^4/12\mu d}, \end{aligned} \quad (13)$$

and the resulting nondimensional parameters are

$$\begin{aligned} R_{\text{out}}^* &= \frac{R_{\text{out}}}{d}, & Q_0^* &= \frac{12\mu Q_0 d}{2\pi Gb_0^4}, & \Gamma^* &= \frac{d\gamma}{Gb_0^2}, & C^* &= \frac{Gb_0^3}{12d^2\gamma}, & \mathcal{H}^* &= \frac{\pi}{4} \frac{b_0}{d} \Gamma^*, \\ R_{\text{init}}^* &= \frac{R_{\text{init}}}{d}, & p_a^* &= \frac{p_a}{Gb_0/d}, & V_{\text{init}}^* &= \frac{V_{\text{init}}}{2\pi b_0 d^2}. \end{aligned} \quad (14)$$

Here, R_{out}^* is the nondimensional radius of the elastic slab, or equivalently its aspect ratio, and is assumed to be moderately large, while Q_0^* is a nondimensional flow rate and measures the strength of the FSI in the cell. These two are the main parameters, and also apply to single-phase flow. The

three parameters Γ^* , \mathcal{C}^* , and \mathcal{H}^* are related to the role of surface tension, and are in fact related by $\Gamma^* = (b_0/d)/(12\mathcal{C}^*) = (d/b_0)(4/\pi)\mathcal{H}^*$, so only two of the three are independent.

From here on, we use only nondimensional quantities, dropping the asterisks for simplicity. The resulting nondimensional forms of most of the governing equations (1)–(12) are then obtained by simply setting $12\mu = G = b_0 = d = 1$ and replacing π in Eqs. (9) and (12) by $1/2$. The exceptions are the bubble front conditions (7a), which become

$$(1 - f_1)\dot{R} = -b^2 \frac{\partial p}{\partial r}, \quad p - p_b = -\frac{2\Gamma}{b}(1 + f_2) - \frac{\mathcal{H}}{R} \quad \text{at } r = R^+, \quad (15)$$

with f_1 and f_2 functions of $\text{Ca} = \mathcal{C}\dot{R}$.

We solve this system numerically using first-order implicit integration in time (backward Euler) and second-order finite differences in space; see Appendix for details. We typically terminate the simulation when the distance $R_{\text{out}} - R$ from the bubble to the rim decreases below 0.1, in which case we deem the bubble to be escaping the cell, or when the minimum cell gap

$$b_{\min}(t) = \min_r b(r, t), \quad (16)$$

which typically occurs at a well-defined bulge near the rim, decreases below 0.05, in which case we deem the cell to be choking, as increasingly fine numerical resolution in space and time would be required to resolve the flow past these thresholds. When the cell is deemed to be choking, increasing the resolution of the simulations indicates that b_{\min} continues to decrease, and would reach zero in finite time which traps the bubble in the cell, rather than taking infinite time to decay to zero which might allow the bubble to escape. However, the model becomes invalid when the gap is too small; we discuss this issue further in Sec. VI.

The material parameters used in the experiments by Peng *et al.* [22] correspond to values for the nondimensional parameters in the ranges $4 \leq R_{\text{out}} \leq 25.4$, $0.02 \leq Q_0/R_{\text{out}} \leq 100$, $0.1 \leq \Gamma \leq 2.5$ and $180 \leq p_a \leq 1000$, with \mathcal{C} and \mathcal{H} being related to Γ via the ratio b_0/d which ranged between 0.04 and 0.3. This motivates the parameter values studied in this paper.

III. EXPANSION OF THE BUBBLE BELOW THE CHOKING THRESHOLD

Throughout this section, we focus on the specific value $R_{\text{out}} = 20$ for the cell radius and $Q_0 = 20$ for the nondimensional injection flow rate, which is below $Q_0 \approx 1.4R_{\text{out}}$ at which the single-phase system is expected to choke [16].

A. Review of single-phase flow (no gas)

We first briefly review the single-phase case, in which there is no gas in the system and flow in the liquid-filled cell is driven by injection of more of the same liquid (so that the lubrication equation (6) holds throughout the domain). Figures 3(a) and 3(b) show the cell deformation and pressure at various times from a simulation with $Q_0 = R_{\text{out}} = 20$.

We observe that the solid deformation and flow are initially localized near the cell center (inlet) $r = 0$ and the rim (outlet) $r = R_{\text{out}}$. The injected fluid expands the gap near $r = 0$ and pushes the solid outward, which in turn bulges near the outlet and squeezes fluid out of the cell at the injection rate. As time passes, the deformation of the solid reaches a steady state, with the pressure profile driving a steady flow through the cell. For a rigid cell, the steady-state pressure profile $p = Q_0 \ln(R_{\text{out}}/R)$ would be reached instantaneously [dotted curve in Fig. 3(b)].

The slab deformation is driven by the gradient in normal stress (i.e., pressure) squeezing the solid toward the rim (rather than by the shear stress from the fluid, which is neglected in this model). Away from the injection point and the rim (i.e., at distances larger than the solid thickness, $r \gg 1$ and $R_{\text{out}} - r \gg 1$), the solid can be modeled using a long-wave approximation (analogous to fluid lubrication theory) [16,39], which yields the horizontal displacement profile and the surface

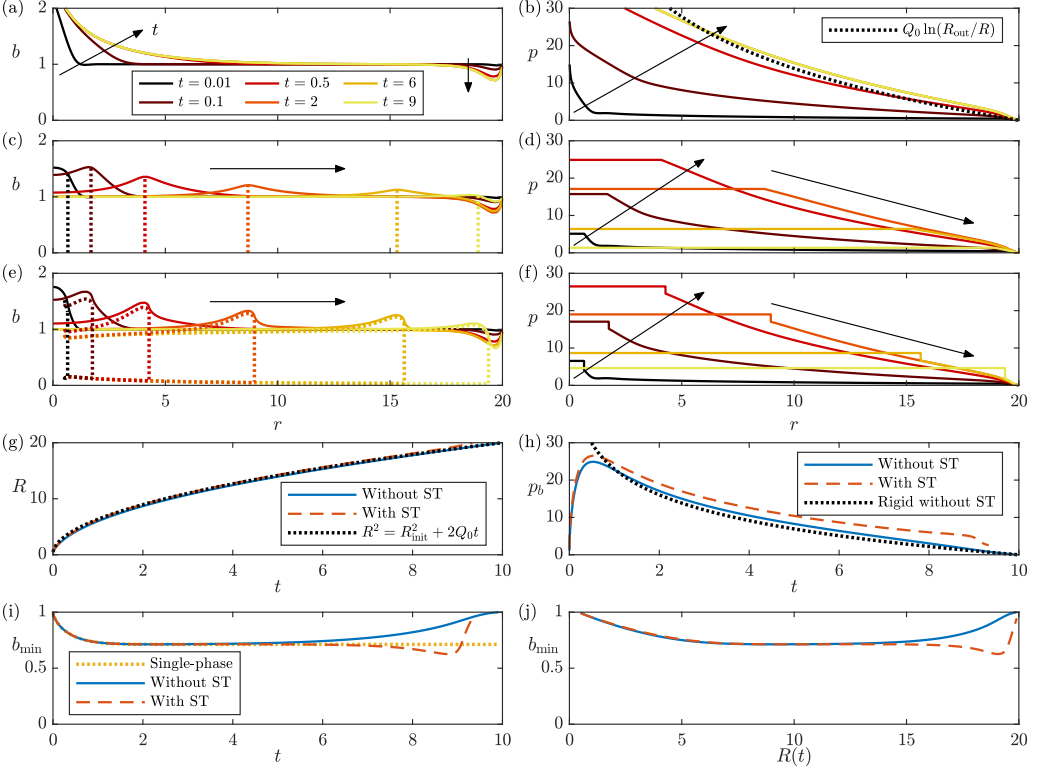


FIG. 3. Numerical results for incompressible flow with $Q_0 = R_{\text{out}} = 20$. Top: Snapshots of channel height/deformation profiles (left) and pressure profiles (right) at various times for (a), (b) single-phase flow, (c), (d) two-phase flow without surface-tension (ST) effects ($\Gamma = \mathcal{H} = \mathcal{C} = 0$), and (e), (f) two-phase flow with surface-tension effects ($\Gamma = 1$, $\mathcal{H} = 0.1\pi/4$, $\mathcal{C} = 0.1/12$). In panel (b), the pressure profile in a rigid cell (dotted curve) is shown for comparison. In panel (c), the vertical dotted lines indicate the position of the displacement front. In panel (e), the dotted curves correspond to the bubble boundary, indicating both the position of the displacement front and the thickness of the residual films. Bottom: Time evolution of (g) the bubble radius R , (h) the bubble pressure p_b , and (i) the minimum cell gap b_{min} , as well as (j) b_{min} plotted against R , from panels (c)–(f). In panels (g), (h), results from a rigid cell with no surface tension are shown for comparison. In panel (i), single-phase results from panels (a), (b) are also shown.

deflection

$$\mathbf{u}_H^s \approx -\frac{1-z^2}{2} \nabla_H p, \quad w \approx -\nabla_H \cdot \left(\frac{1}{3} \nabla_H p \right). \quad (17)$$

This explains the somewhat surprising result that there is negligible vertical deflection, $w \ll 1$, for intermediate values of r in Fig. 3(a), as the harmonic pressure field results in zero vertical deflection and a steady flow. As a result, the steady-state pressure profile in the approximately flat part of the elastic cell differs from that in a rigid cell by an additive constant, corresponding to the additional pressure drop due to the constriction near the rim.

B. Two-phase flow with incompressible gas

We now consider the injection of gas. We first neglect any effects of gas compression by imposing the incompressible injection law (10), and compare the single-phase case discussed previously with a two-phase simulation without surface-tension effects ($\Gamma = \mathcal{H} = \mathcal{C} = 0$) and a two-phase

simulation with surface-tension effects ($\Gamma = 1$, $\mathcal{H} = 0.1\pi/4$ and $\mathcal{C} = 0.1/12$ corresponding to a dimensional ratio $b_0/d = 0.1$).

With no surface tension [Figs. 3(c) and 3(d)], the gap initially expands near the center and constricts near the rim, as in the single-phase case, and the pressure profiles are similar outside of the bubble region. As the bubble grows outward, the cell relaxes toward its undeformed state behind the advancing bubble front [the long-wave approximation (17) for the solid yields $w \approx 0$ for a spatially uniform pressure $p = p_b$]. A localized region of expansion travels with the bubble front, with the solid being squeezed toward the rim on the liquid side while not being squeezed in either direction on the gas side. Near the rim, the bulge initially grows (or equivalently the minimum cell gap b_{\min} decreases) and then approaches a steady state [Fig. 3(i)], just like for single-phase flow. However, as the bubble approaches (i.e., $R \rightarrow R_{\text{out}}$), the size of the liquid region (over which the solid is being squeezed toward the rim by the viscous pressure gradient) reduces, and hence the solid starts to relax [Fig. 3(j)]. This is the key mechanism by which the inviscid bubble, due to its proximity to the rim, mitigates the tendency of the system to choke. We will revisit it later in Sec. IV A.

The time evolution of the bubble radius R [Fig. 3(g)] closely follows the prediction from a rigid cell, in which conservation of volume yields $R^2 = R_{\text{init}}^2 + 2Q_0t$. This is because the deformation of the soft cell has a relatively small effect on the distribution of the fluids. The bubble pressure p_b [Fig. 3(h)] initially increases as the bulge gap constricts near the rim, but eventually decreases as more and more viscous liquid is replaced by inviscid gas. Due to the constricting bulge near the rim, the pressure remains slightly above the value $p_b = Q_0 \ln(R_{\text{out}}/R)$ it would have in a corresponding rigid-walled cell.

When we include surface tension in the model [Figs. 3(e) and 3(f)], the pressure has a capillary jump at the bubble front (controlled by Γ and \mathcal{H}), which changes the deformation profile in its vicinity. The pressure jumping from a higher value in the bubble to a lower value in the liquid causes the gap to expand immediately behind the bubble front and contract immediately ahead of it [Fig. 3(e)], as compared with the profile near the interface without surface tension [Fig. 3(c)]. When the bubble approaches the rim, the bulge initially grows slightly due to the pressure jump, before it relaxes due to the reduction in size of the liquid region [Figs. 3(i) and 3(j)].

The evolution of the bubble radius [Fig. 3(g)] changes slightly due to the change in the cell deformation, and also because of the thin residual liquid films being deposited on the cell walls [Fig. 3(e)], controlled by the parameter \mathcal{C} . Finally, the bubble pressure [Fig. 3(h)] is larger compared with the simulation without surface tension because of the capillary pressure jump.

C. Two-phase flow with compressible gas

Next we turn our attention to the effects of the gas compression. As can be seen from equations (11), compression of the gas simply alters the rate of change of the bubble volume, $Q(t)$, so that it deviates from the nominal value Q_0 that is imposed by injection. As a result, the mechanisms for the deformation of the cell, discussed above, remain largely unchanged, but the dynamics of the system may be affected by the varying flow rate $Q(t)$.

For simplicity, we neglect the effects of surface tension (i.e., set $\Gamma = \mathcal{H} = \mathcal{C} = 0$), and consider a few different values of the atmospheric pressure p_a . The results of our numerical simulations are shown in Fig. 4, in which we plot the time-evolution of the bubble radius $R(t)$, the rate of change $Q(t)$ of the bubble volume in the cell, the bubble pressure $p_b(t)$ and the minimum cell gap $b_{\min}(t)$, for injection using either a syringe pump (left column) or a pressurized bottle (right column). We note that, despite the different governing equations (11) and initial gas volumes (12), the two injection methods produce qualitatively similar results.

For large p_a , which corresponds to the typical gauge pressure in the cell being small compared with atmospheric pressure, the effect of gas compression is negligible: The flow rate $Q(t)$ is approximately equal to the nominal value Q_0 , and the evolution of the bubble radius R , bubble pressure p_b and minimum cell gap b_{\min} follow the results from the incompressible model.

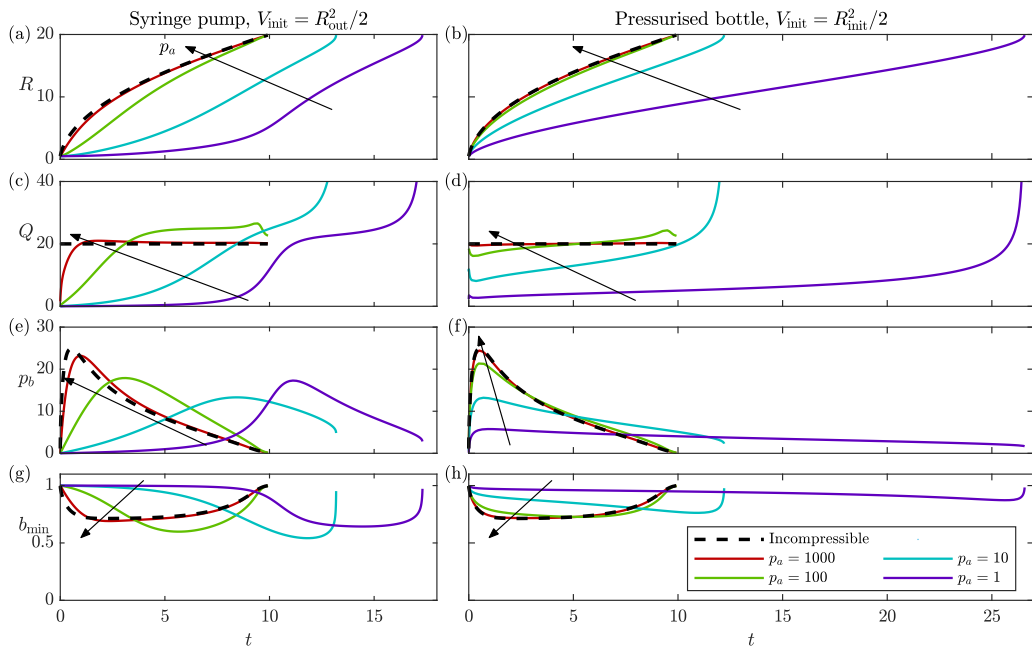


FIG. 4. Numerical simulations with gas compression using the two injection models (11), for nominal flow rate $Q_0 = R_{\text{out}} = 20$ and four values of the atmospheric pressure parameter p_a , without surface tension. Time evolution of (a), (b) the bubble radius R , (c), (d) the liquid flow rate Q exiting the cell, (e), (f) the bubble pressure p_b , and (g), (h) the minimum cell gap b_{min} . Results from an incompressible simulation (10), which corresponds to $p_a \rightarrow \infty$, are shown for comparison.

As p_a is reduced, the effect of compression becomes significant: The injection initially drives only a small fluid flow $Q(t)$, while the bubble pressure rises and the gas compresses. As the bubble expands and the amount of viscous fluid in the cell reduces, the resistance to flow in the cell decreases, and the bubble attains a maximal pressure before starting to depressurize. However, if there is any remaining overpressure when the bubble reaches the rim, then the flow rate diverges. Also, for larger compressibility (lower p_a), the bubble reaches the rim later. These results are qualitatively similar to those in a rigid cell [36] or a rigid capillary tube [35]. In particular, for a rigid cell with large $V_{\text{init}} \gtrsim R_{\text{out}}^2/2$, the compressibility number defined by Cuttle *et al.* [36] is, after the nondimensionalization in Eq. (14), $C = 4Q_0V_{\text{init}}/(R_{\text{out}}^2p_a)$, and is the main parameter that predicts whether the flow rate diverges ($C > 1$) or not ($C \lesssim 1$) as $R \rightarrow R_{\text{out}}$ in Fig. 4(c).

The reduction in flow rate due to gas compression initially is the second key mechanism by which the bubble can mitigate the tendency of the system to choke. This will be explored further in Sec. IV B.

IV. THE EFFECTS OF THE BUBBLE ON CHOKING

A. The proximity of the bubble to the rim

We assess how choking is influenced by the proximity of the inviscid gas bubble to the cell rim by studying the system at a larger flow rate, $Q_0 = 29 = 1.45R_{\text{out}}$, that is slightly above the single-phase choking threshold of $Q_0 \approx 1.4R_{\text{out}}$ [16]. For simplicity, we once again neglect gas compression and surface tension. The evolution of the gap profile near the rim is plotted in Fig. 5(a): The bulge grows in amplitude and approaches the opposite wall as the minimum gap b_{min} shrinks toward zero. In this case, for which the bubble has initial radius $R_{\text{init}} = 0.5$, the bulge develops and the cell chokes

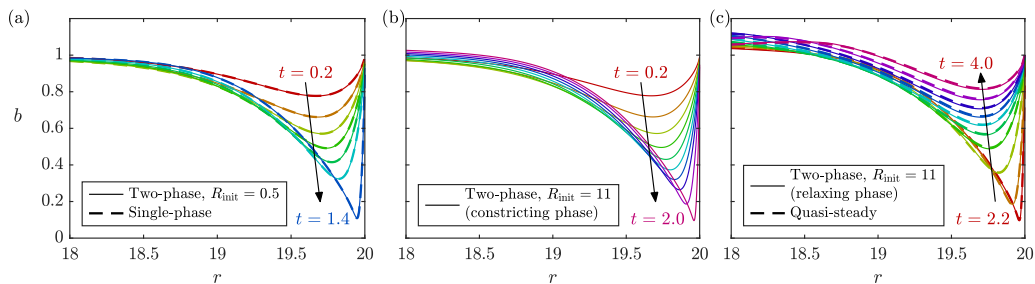


FIG. 5. Numerical results for the channel gap profile $b(r, t)$ near the cell rim, for incompressible flow with flow rate $Q_0 = 29 = 1.45R_{\text{out}}$, which is slightly above the single-phase choking threshold, without surface tension. Snapshots are shown with nondimensional time increments of 0.2 from the first to last times indicated, and two different values of the initial bubble radius R_{init} are considered. (a) $R_{\text{init}} = 0.5$, with single-phase results shown for comparison. (b), (c) $R_{\text{init}} = 11$, split between (b) the constricting phase and (c) the relaxing phase, with quasisteady profiles with the same radius and pressure drop shown for comparison in panel (c).

before the displacement front is near enough to the rim to have any mitigating effect. Indeed, the profiles agree closely with analogous ones from a single-phase simulation (dashed curves).

Profiles from a simulation with larger initial bubble radius, $R_{\text{init}} = 11$, are shown in Figs. 5(b) and 5(c). The bulge initially grows [Fig. 5(b)] and the channel nearly chokes. However, as the bubble grows, it reduces the amount of liquid that is squeezing the solid toward the rim. This reopens the channel [Fig. 5(c)] and choking is averted.

To illustrate how the presence of the bubble near the rim helps the bulge to relax and therefore reduces the tendency of the system to choke, we consider how the bulging changes for different values of the initial bubble radius R_{init} . Figure 6(a) shows the time evolution of the minimum cell gap b_{min} , and the same data is plotted in Fig. 6(b) as a function of the interface position R . For $R_{\text{init}} \lesssim 10$, the bubble does not arrive at the rim early enough to mitigate choking, so b_{min} shrinks steadily to zero, reaching it at a finite value of $R < R_{\text{out}}$. As a result, the system chokes around $t \approx 1.5$, just like in the single-phase case [dashed curve in Fig. 6(a)]. For $R_{\text{init}} \gtrsim 11$, b_{min} initially

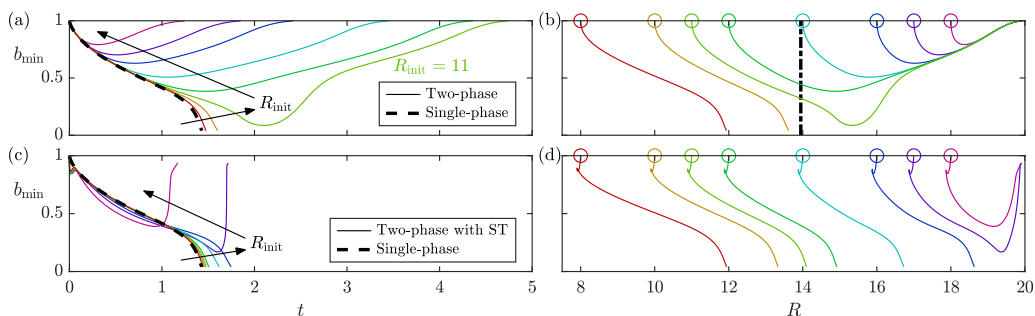


FIG. 6. Numerical results for the evolution of the minimum cell gap b_{min} , for incompressible flow with flow rate $Q_0 = 29 = 1.45R_{\text{out}}$, which is slightly above the single-phase choking threshold. The evolution is plotted as a function of (a), (c) time t and of (b), (d) the bubble radius R for the two-phase case (a), (b) without surface tension and (b), (d) with surface tension ($\Gamma = 1$, $\mathcal{H} = 0.1\pi/4$, $\mathcal{C} = 0.1/12$). Different colors correspond to different initial values $R_{\text{init}} = 8, 10, 11, 12, 14, 16, 17, 18$, as indicated by the circles in panels (b), (d). The curve corresponding to the profiles shown in Figs. 5(b) and 5(c) is labeled as $R_{\text{init}} = 11$ in panel (a). The single-phase result is also shown for comparison in panels (a), (c). In panel (b), the vertical dash-dotted line shows the choking boundary predicted by the quasisteady analysis [Eq. (18)].

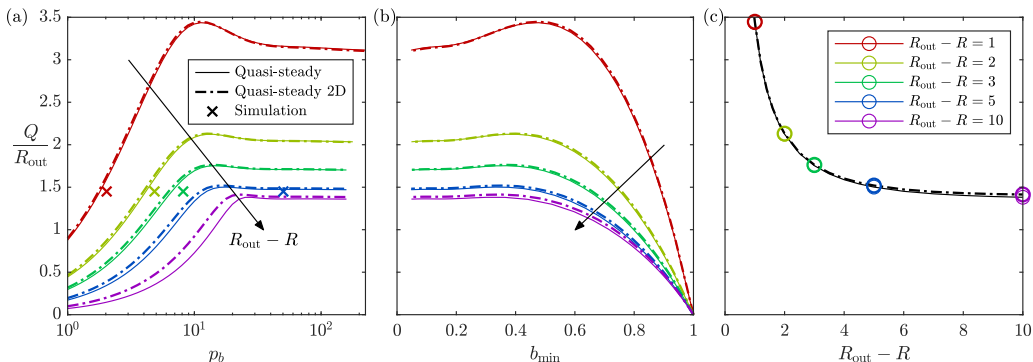


FIG. 7. Numerical results from the quasisteady approximation (18), for $R_{\text{out}} = 20$ and without surface tension. The scaled flow rate Q/R_{out} is plotted as a function of (a) bubble pressure p_b and (b) minimum cell gap b_{min} , for various values of the bubble distance from the rim $R_{\text{out}} - R$. The color-coding is explained with the legend in panel (c). (c) The maximal Q/R_{out} plotted as a function of $R_{\text{out}} - R$. In all panels, analogous results for a two-dimensional cell are plotted with dash-dotted curves. In panel (a), crosses indicate the values of p_b and Q/R_{out} at the various distances in the time-evolving simulation from Figs. 5(b) and 5(c).

shrinks, but does not vanish before the bubble is close enough to mitigate the bulge; thereafter, b_{min} returns to one instead of decaying to zero.

Figures 6(c) and 6(d) show analogous simulations with surface-tension effects. The capillary pressure drop across the bubble front constricts the gap in front of the bubble (and expands it behind) [see Fig. 3(e)] which partly offsets the relaxing effect of the bubble on choking. Hence, the bubble needs to be closer to the rim to prevent b_{min} decreasing to zero. In these simulations, the system chokes for $R_{\text{init}} \lesssim 16$ and only avoids choking for $R_{\text{init}} \gtrsim 17$. We do not study the effects of surface tension further.

A further observation that can be made in Fig. 6(b) is that when the bubble approaches the rim, the curves from different simulations collapse onto a universal curve, indicating that the deformation profile becomes approximately independent of the initial conditions, and instead only depends on the current bubble front position R (as well as the flow rate and the material parameters). We calculate an ad-hoc approximation of this profile by seeking quasisteady solutions of the governing equations: we neglect the time derivative \dot{h} in the lubrication equation (6) and fix the position of the bubble front R instead of evolving it using Eq. (7a). Thus, we solve the remaining governing equations from Eqs. (1)–(9) together with

$$0 = \nabla \cdot (b^3 \nabla p) \quad \text{in } r > R, \quad \text{where } R \text{ is fixed.} \quad (18)$$

The resulting deformation profiles at given values of R [dashed curves in Fig. 5(c)] are in excellent agreement with those obtained from the time-evolving simulation, provided that we impose the same bubble pressure p_b , rather than the same flow rate Q .

In this quasisteady model, any one of Q , p_b , and b_{min} can be treated as the control parameter. We have chosen to perform the quasisteady calculations for a range of values of the bubble front position R and total pressure drop across the liquid region (or, equivalently, the bubble pressure p_b) rather than Q to avoid the issue of multiple solution branches existing for Q just below the maximum value. Fig. 7 shows how the scaled flow rate Q/R_{out} in the quasisteady solutions depends on p_b , b_{min} , and R . For each value of R , we see in Fig. 7(a) that increasing p_b initially drives more flow Q , but due to the bulge constricting the channel, Q reaches a maximum and then remains near the maximum as p_b increases further. We also plot the relationship between b_{min} and Q [Fig. 7(b)], and find similarly that a decrease in b_{min} from 1 initially corresponds to an increase in Q , but once the same maximum in Q is reached, the flow rate remains near it as b_{min} decreases further.

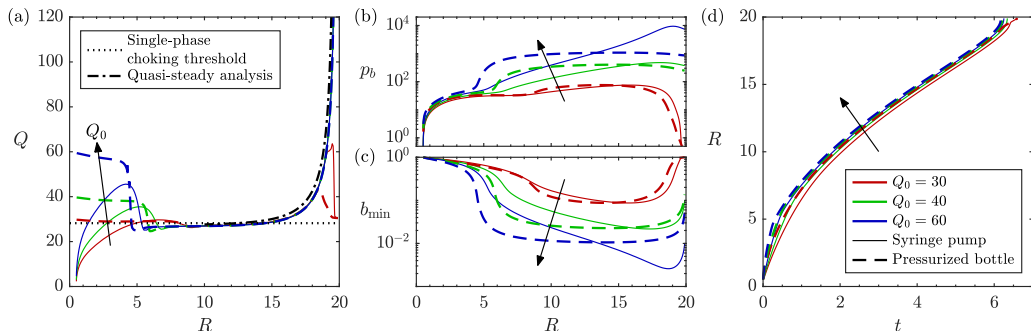


FIG. 8. Simulations in the near-choking regime, for $R_{\text{out}} = 20$ and three values of the nominal injection flow rate Q_0 above the single-phase choking threshold: Evolution of the (a) resulting flow rate Q , (b) bubble pressure p_b , and (c) minimum cell gap b_{\min} as functions of the bubble radius R , and (d) of R as function of t . The simulations assume gas compressibility ($p_a = 1000$) and two injection methods (syringe pump with $V_{\text{init}} = R_{\text{out}}^2/2$ or pressurized bottle with $V_{\text{init}} = R_{\text{init}}^2/2$, shown with solid and dashed curves, respectively), but no surface-tension effects ($\Gamma = \mathcal{H} = \mathcal{C} = 0$). In (a), the choking threshold for the single-phase flow and results from the quasisteady analysis [Fig. 7(c)] are shown for comparison.

We can compare these computations to the results shown in Fig. 5(c), in which the flow rate is $Q_0 = 1.45R_{\text{out}}$. For each value of R plotted in Fig. 7(a), we extract the corresponding values of p_b from the time-evolving simulation in Fig. 5(c) and mark them with crosses in Fig. 7(a). This comparison reveals a small but noticeable difference between the flow rate predicted by the quasisteady solution and the flow rate obtained in the time-evolving simulations, despite the excellent agreement in deformation profiles observed in Fig. 5(c).

As described by Box *et al.* [16], in the single-phase case, the occurrence of choking in time-evolving simulations with an imposed flow rate Q_0 is linked to the lack of existence of a steady state with flow rate $Q = Q_0$. Analogously, for each value of R we can identify the largest flow rate Q for which a quasisteady solution exists. The resulting curve [Fig. 7(c)] represents an approximate boundary, beyond which the large flow rate in the channel is unsustainable and the system is expected to choke. When evolving from an initially undeformed state, which corresponds to $R_{\text{out}} - R$ decreasing as the bubble grows, the system thus avoids choking if the bubble manages to cross the boundary shown in Fig. 7(c) before the bulge has had time to grow and make contact with the opposite wall. For example, the boundary for $Q/R_{\text{out}} = 1.45$ is at $R_{\text{out}} - R \approx 6$, i.e., $R \approx 14$, and indeed as seen in Fig. 6(b) where this boundary is indicated by the vertical dash-dotted line, in the cases where the cell choked, it did so before the bubble reached $R \approx 14$, while if the bubble did reach $R \approx 14$ then it went on to escape without the cell choking.

The dash-dotted curves in Fig. 7 show the results of the quasisteady calculations for a two-dimensional cell, in which Q/R_{out} corresponds to the flow rate per unit length in the third, Cartesian, dimension. The two-dimensional results agree well with the radial results, especially for small $R_{\text{out}} - R$, since the dynamics are limited to the region near the rim where the difference between radial and two-dimensional geometry is small. Hence, the results in Fig. 7 are expected to apply for other cell sizes $R_{\text{out}} \gg 1$, not just the value $R_{\text{out}} = 20$ considered here.

B. The near-choking regime for compressible gas

We now investigate the impact of gas compression on choking, by considering injection with nominal flow rates $Q_0/R_{\text{out}} = 1.5, 2, 3$ and an atmospheric pressure parameter of $p_a = 1000$. To aid the discussion, we plot the flow rate Q , bubble pressure p_b and minimum cell gap b_{\min} as functions of the interface position R in Figs. 8(a)–8(c).

As evident from Fig. 8(a), the flow rate can transiently exceed the critical value for the single-phase flow $Q(t) \approx 1.4R_{\text{out}}$ [horizontal dotted line in Fig. 8(a)] at early times. However, once the bulge has grown large enough to significantly constrict the gap [see also Fig. 8(c)], the flow rate rapidly drops to this critical value. The mismatch between the larger flow rate Q_0 of gas injection and the smaller flow rate $Q(t)$ of liquid exiting the cell is accommodated by volumetric compression of the gas, which causes the gas pressure to increase continually. This in turn reduces the cell gap further [Figs. 8(b) and 8(c)]. Nevertheless, the flow rate does not change significantly, consistent with Q reaching a plateau as $p_b \rightarrow \infty$ or $b_{\text{min}} \rightarrow 0$ in the quasisteady solutions in Figs. 7(a) and 7(b). As the bubble approaches the rim, the maximum sustainable flow rate increases [Fig. 7(c)] and the flow rate follows this increase [dash-dotted curve in Fig. 8(a)]. [For Q_0 just above the single-phase choking threshold, such as $Q_0 = 30$ in Fig. 8(a), the flow rate stops increasing as the bubble decompresses before escaping the cell, but for larger Q_0 the pent up pressure allows the flow rate $Q(t)$, and the bubble velocity $\dot{R}(t)$, to diverge in this model as $R \rightarrow R_{\text{out}}$, as discussed at the end of Sec. III C.]

We conclude that for nominal flow rates above the choking threshold, gas compression enables the system to enter a “near-choking” regime after the initial transient. In this regime, the flow rate follows the threshold curve in Fig. 7(c), which is a function of the bubble front position R , but does not depend on the injection flow rate. A consequence of this is that the simulations with different Q_0 and different injection mechanisms all have approximately the same flow rate $Q(t)$ during the main part of the simulation, and hence the time evolution of the bubble radius $R(t)$ is approximately the same between all of them [Fig. 8(d)].

We note that compression plays an important role despite the large value of $p_a = 1000$ (for which compressive effects were weak in Fig. 4). Indeed, in the absence of compression, the flow rate $Q(t) = Q_0$ would be sufficiently large for the cell to choke; the minimum cell gap would decrease from its initial value $b_{\text{min}} = 1$ toward zero, becoming arbitrarily small in finite time [Fig. 5(a)]. However, as the minimum gap narrows, the viscous resistance (both to flow through the narrow gap and to further reduction of the gap) requires the pressure in the bubble to increase without bound if the flow rate Q_0 is to be sustained. As a consequence, no matter how small the compressibility of the gas is, it must compress, which reduces the flow rate $Q(t)$, so that the cell does not choke. Therefore, given that a real gas is never perfectly incompressible, one would expect no choking to occur in experiments. We discuss this apparent contradiction further in Sec. VI.

V. THE DYNAMICS OF THE ADVANCING BUBBLE FRONT

It is possible to elaborate on the dynamics of the advancing bubble front under the assumption that $R \gg 1$ and $R_{\text{out}} - R \gg 1$, i.e., the bubble and liquid regions have horizontal extents that are large compared with the solid thickness. The elastic equations for the solid in those regions can then be approximated by the long-wave result (17) which yields $w \approx 0$ in both the liquid region [16] and the bubble region. However, the approximation does not apply near the cell rim or near the bubble front, where the horizontal length scale of variation becomes comparable to the solid thickness. Since in this asymptotic regime the bubble is far away from the rim, the deformation near the rim is well described by the single-phase local boundary-layer solution calculated by Box *et al.* [16]. Here we study the local behavior near the bubble front using a traveling-wave approximation.

A. Traveling-wave equations

We define a local co-moving coordinate $x = r - R(t)$ which is assumed to be $O(1)$. Substituting into the elastic equations (1) and neglecting quantities of order $R^{-1} \ll 1$, we obtain the two-dimensional equations

$$\sigma_{xx}^s = -p^s + 2\partial_x u_x^s, \quad \sigma_{zz}^s = -p^s + 2\partial_z u_z^s, \quad \sigma_{xz}^s = \sigma_{zx}^s = \partial_z u_x^s + \partial_x u_z^s, \quad (19a)$$

$$\partial_x u_x^s + \partial_z u_z^s = 0, \quad 0 = \partial_x \sigma_{xx}^s + \partial_z \sigma_{zx}^s = \partial_x \sigma_{xz}^s + \partial_z \sigma_{zz}^s. \quad (19b)$$

Under the traveling-wave approximation that the deformation profile is steadily translating with the bubble front $R(t)$, i.e., $\dot{w} \approx -\dot{R}w'$, where prime denotes a derivative with respect to x , the lubrication equation (6) can be integrated to

$$-\dot{R}w = (1+w)^3 p' + q \quad \text{in } x > 0, \quad (20)$$

where q is a constant of integration. Equation (5) for the bubble pressure remains as $p = p_b(t)$ in $x < 0$, and the bubble-front conditions (7a) become

$$[1 - f_1(C\dot{R})]\dot{R} = -b^2 p', \quad p - p_b = -\frac{2\Gamma}{b}[1 + f_2(C\dot{R})] \quad \text{at } x = 0^+, \quad (21)$$

while the conditions on the top and bottom surface of the elastic solid remain as

$$\mathbf{u}^s|_{z=1} = \mathbf{0}, \quad w = u_z^s|_{z=0}, \quad p = -\sigma_{zz}^s|_{z=0}, \quad 0 = \sigma_{xz}^s|_{z=0}. \quad (22)$$

This is a local analysis near $r = R$, so the injection and rim conditions (9)–(11) are irrelevant. Instead we match to the long-wave structure (17) at large $\pm x$, by imposing

$$w, u_z^s \rightarrow 0 \quad \text{as } x \rightarrow \pm\infty, \quad u_x^s \rightarrow 0 \quad \text{as } x \rightarrow -\infty, \quad u_x^s \rightarrow \frac{1-z^2}{2}q \quad \text{as } x \rightarrow \infty, \quad (23)$$

where we identify $q = -\lim_{x \rightarrow \infty} p'$ to be the far-field flux or negative pressure gradient. Since the value of p_b simply changes p by a constant, we only need to solve the equations above for $p_b = 0$.

Solving these equations determines the unknown advancement velocity \dot{R} of the bubble, which depends on the nondimensional surface-tension parameters Γ and C and the far-field flux q . However, for convenience, we instead proceed by imposing the value of \dot{R} and solving the equations numerically (using Newton iteration) to obtain q as a function of \dot{R} . Another important quantity is the effective additional pressure drop in the local region (as compared with an undeformed cell, in which the pressure gradient would be a constant q , with no capillary pressure drop),

$$\Delta p = p_b - \lim_{x \rightarrow \infty} (p + qx). \quad (24)$$

This is also calculated numerically as a function of \dot{R} .

B. No residual films

We first consider the case when no residual films are deposited on the walls behind the advancing bubble front, which corresponds to $C = 0$. In this case, combining the traveling-wave lubrication equation (20) with the kinematic boundary condition (21) yields the relationship

$$q = \dot{R}, \quad (25)$$

meaning that the steady advancement velocity of the bubble must be equal to the depth-averaged lubrication velocity far ahead of the bubble, since liquid volume is conserved.

Channel height profiles for various values of \dot{R} are plotted in Fig. 9(a) for the case of no surface tension. As was discussed in Sec. III B, an advancing bubble is associated with a liquid pressure gradient in $x > 0$ that squeezes the solid away from the bubble and dilates the gap. Results are also included for retreating bubbles ($\dot{R} < 0$), in which case the elastic solid is squeezed toward the bubble and constricts the gap. As \dot{R} decreases toward a critical value just below -5 , the minimum cell gap shrinks toward zero, and no solutions are found for lower values of \dot{R} , indicating an alternative mechanism for choking, in which liquid displacing gas at sufficiently large flow rate causes the elastic solid to make contact with the opposite wall near the moving interface (rather than near the rim of the cell).

Adding in a static capillary pressure drop $\Gamma = 1$ across the bubble front [Fig. 9(b)] results in a relative constriction of the gap ahead of the bubble front and a dilation behind the bubble front, as discussed in Sec. III B

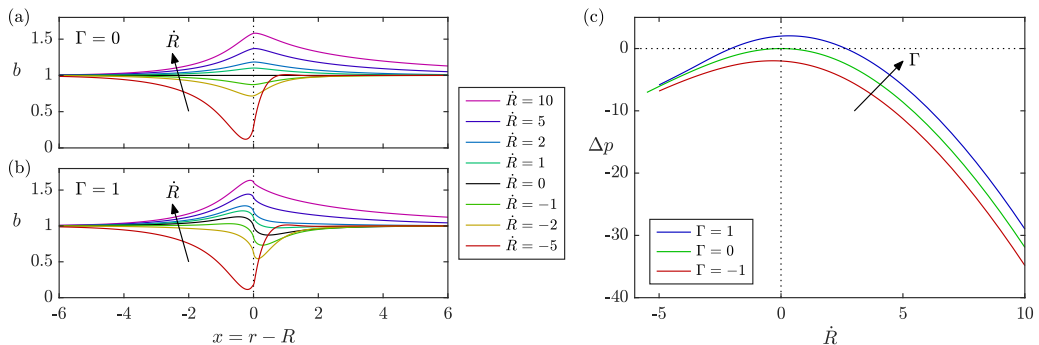


FIG. 9. Numerically calculated traveling-wave solutions with no residual films ($\mathcal{C} = 0$). (a), (b) Cell gap profiles for various bubble advancement velocities \dot{R} and two values of the surface-tension parameter Γ . The location $x = 0$ of the bubble front is indicated with a vertical dotted line. (c) The local additional pressure drop as a function of velocity \dot{R} for three values of Γ .

The local additional pressure drop in the traveling-wave region is plotted in Fig. 9(c) as a function of the bubble front velocity \dot{R} for various values of the surface-tension parameter Γ . (It is possible to generalize the definition of Γ to include cases of partial wetting with a contact angle θ_c , for which Γ is modified by a factor $\cos \theta_c$ and can therefore be negative.) For the static case $\dot{R} = 0$, the additional pressure drop is simply given by the static formula $\Delta p = 2\Gamma$ (the static deformation profile is an odd function of x , so $b = 1$ at the bubble front). For $\dot{R} > 0$, the gap expands and the viscous pressure drop reduces, resulting in a smaller Δp . Similarly, for $\dot{R} < 0$, the gap constricts and the viscous pressure drop increases, but due to the reversed flow direction we again obtain a smaller Δp .

C. With residual films

We now consider the case of nonzero \mathcal{C} , representing the deposition of thin liquid films on the cell walls behind the advancing bubble front. Combining Eq. (20) with Eq. (21) now yields a more complicated relationship between the far-field flux q and the advancement velocity \dot{R} , which we can express in terms of the total thickness m of films deposited on the walls as

$$q = (1 - m)\dot{R}, \quad m = f_1(\mathcal{C}\dot{R})b|_{x=0}. \quad (26)$$

Examples of resulting channel height profiles are plotted in Figs. 10(a)–10(c), with the thin curves in the bubble region $x < 0$ showing the residual liquid films of thickness $m/2$ coating each wall. As \dot{R} increases, both the film correction factor $f_1(\mathcal{C}\dot{R})$ and the cell gap $b|_{x=0}$ increase, which results in the residual film thickness m increasing and the ratio q/\dot{R} decreasing. For small and moderately large \dot{R} , for which m is not too close to 1, the bubble continues to push a significant amount of liquid ahead of it, with the far-field flux being $q = O(\dot{R})$ [Fig. 10(d)]. However, as m approaches 1, the bubble transitions to “peeling” the two walls apart while leaving the fluid mostly in place as two thick films coating the walls [Fig. 10(c)]. This allows the advancement velocity to become much larger than the far-field flux [Fig. 10(e)]. (In practice, for large \dot{R} , rather than settling into a steadily translating state, the system might exhibit unsteady dynamics such as repeated pinch-off of bubbles as the residual films make contact and reconnect, and become more susceptible to instability in the third dimension.)

In Fig. 10(f) we plot the local additional pressure drop as a function of \dot{R} . For the same value of \dot{R} , the flow rate q is lower [Eq. (26)] compared with the case without films [Eq. (25)], and hence the effect of the deformation of the cell on the pressure drop is also reduced. Therefore, for the same value of \dot{R} , the magnitude of the local additional pressure drop can be significantly smaller in

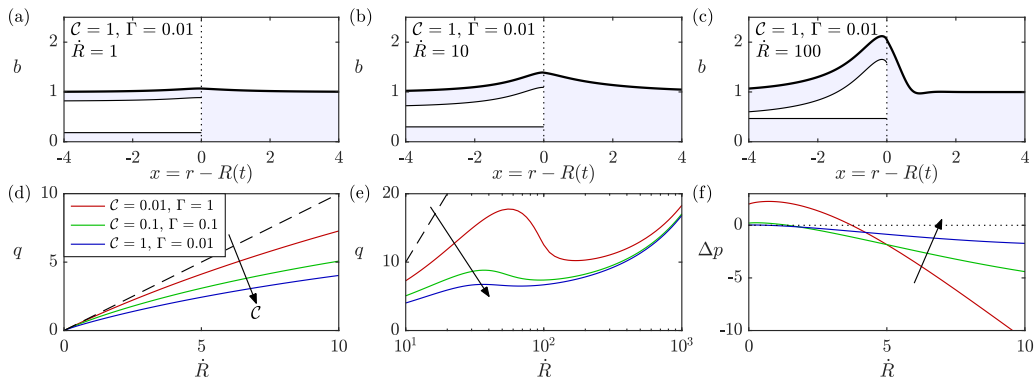


FIG. 10. Numerically calculated traveling-wave solutions for an advancing bubble front that leaves behind liquid films on the cell walls. Top row: Deformation profiles (thick lines) and residual film thicknesses (thin lines) for $\mathcal{C} = 1$, $\Gamma = 0.01$, and three values of the front velocity: (a) $\dot{R} = 1$, (b) $\dot{R} = 10$, and (c) $\dot{R} = 100$. Bottom row: The (d), (e) far-field flux q and (f) local additional pressure drop Δp as functions of \dot{R} for three different values of (\mathcal{C}, Γ) corresponding to a dimensional ratio $b_0/d = 0.12$. In panels (d), (e), the result (25) for $\mathcal{C} = 0$ (and any value of Γ) is shown (dashed line) for reference.

the case with films compared to the case without films [compare Fig. 10(f) with Fig. 9(c) at, e.g., $\dot{R} = 10$].

D. Comparison with numerical simulations

To apply the traveling-wave analysis to the time-evolving problem, we combine it with the long-wave approximation in the liquid region and the local single-phase bulge solution near the rim. In the long-wave liquid region, we have $w = 0$ and hence, by conservation of volume, $\nabla_H^2 p = 0$. This results in

$$p = Q \ln \frac{R_{\text{out}}}{r} + \Delta p_{\text{bulge}}(Q/R_{\text{out}}), \quad (27)$$

where the additional pressure drop Δp_{bulge} near the rim due to the bulging is a function of the local flux Q/R_{out} and can be extracted from the local two-dimensional solutions of Box *et al.* [16]. From this, we can deduce the value of the matching quantity $q = q_{\text{front}}(\dot{R})$, and express the bubble pressure in terms of the matching quantity $\Delta p = \Delta p_{\text{front}}(\dot{R})$,

$$q_{\text{front}}(\dot{R}) = \frac{Q}{R}, \quad p_b = Q \ln \left(\frac{R_{\text{out}}}{R} \right) + \Delta p_{\text{bulge}}(Q/R_{\text{out}}) + \Delta p_{\text{front}}(\dot{R}). \quad (28)$$

For imposed $Q = Q_0$ and a known initial value of R , the first equation in Eq. (28) can be integrated numerically to yield the evolution of R . For the case of compressible gas injection [Eqs. (11)], or other methods of injection that depend on p_b , the evolution of R is obtained by solving Eq. (28) coupled to the injection condition.

We compare results from the traveling-wave analysis with results from a time-evolving simulation, focusing on a case with no gas compression, moderate effects of surface tension and thin films ($\Gamma = 0.1$, $\mathcal{H} = 0.01\pi/4$ and $\mathcal{C} = 1/12$, corresponding to a dimensional ratio $b_0/d = 0.1$), and three different values of the cell radius, $R_{\text{out}} = 5, 10, 20$ (Fig. 11). Figure 11(a) shows the velocity \dot{R} of the bubble front, as a function of its position R , comparing the values obtained in the simulations (solid curves) to the predictions from the traveling-wave analysis (dashed curves). As expected, there is good agreement between the two for $R_{\text{out}} = 20$ and intermediate values of R , when the bubble front is far away from the center and the rim of the cell so that the long-wave approximation holds. For the smaller values of R_{out} , the bubble cannot be as far away from both regions of the cell, so the

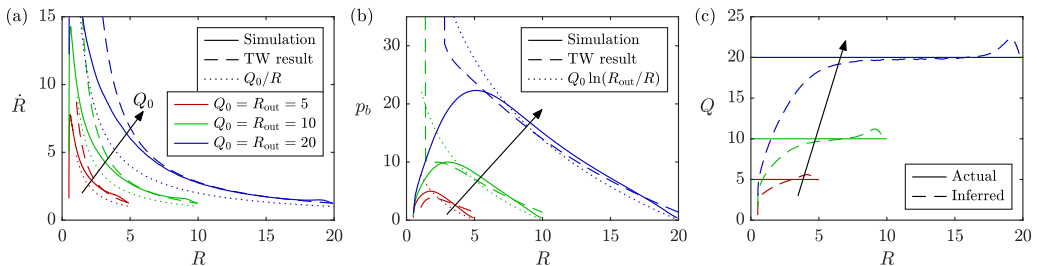


FIG. 11. Application of traveling-wave results to the time-evolving problem, with three values of $Q_0 = R_{\text{out}}$, no gas compression and $\Gamma = 0.1$, $\mathcal{H} = 0.01\pi/4$, $C = 1/12$. The evolution of the bubble (a) front velocity \dot{R} and (b) pressure p_b , as a function of its position R , obtained in the simulations and using the traveling-wave approximation (28). The results $\dot{R} = Q_0/R$ and $p_b = Q_0 \ln(R_{\text{out}}/R)$ for a bubble without surface tension in a rigid cell are also shown. (c) The imposed flow rate of liquid exiting the cell and the flow rate inferred by applying the traveling-wave analysis to the $R = R(t)$ data from the simulations.

agreement is worse. For comparison, the dotted curves show the prediction without residual films [Eq. (25)], i.e., $q_{\text{front}}(\dot{R}) = \dot{R}$, which is noticeably different. Fig. 11(b) shows the bubble pressure p_b as a function of R . Once again, the agreement between simulations and predictions is the best for large R_{out} .

The traveling-wave results can also be used to infer the flow rate $Q = q_{\text{front}}(\dot{R})R$ from the evolution of $R(t)$. Figure 11(c) shows the results (dashed curves) when applied to the data from the simulations in Figs. 11(a) and 11(b). The best agreement with the true value of Q (solid lines) is obtained for large R_{out} , as expected.

VI. DISCUSSION

We have presented and analysed an axisymmetric model for injection of a gas bubble into a liquid-filled elastic-walled Hele-Shaw cell bounded by a confined incompressible elastic solid (Fig. 1). For injection of the same viscous liquid rather than gas, the cell is known to choke for flow rates exceeding a critical value. This choking occurs because the pressure gradient of the viscous flow squeezes the elastic solid toward the rim, where it bulges into the channel and makes contact with the opposite wall [16].

We have identified two mechanisms by which injection of a gas bubble instead of viscous liquid reduces the tendency of the cell to choke. First, for a given flow rate, the proximity of the inviscid bubble to the cell rim reduces the size of the liquid region over which the cell is being squeezed toward the rim by the viscous pressure gradient. Using a quasisteady analysis, we have obtained an approximation for the increased choking threshold as a function of the distance from the bubble to the rim [Fig. 7(c)]. (The surface tension of the bubble can counteract this effect slightly, due to the capillary pressure drop causing a constriction of the cell ahead of the bubble, which warrants further investigation.) Second, compression of the gas reduces the flow rate of the liquid, and since choking requires the pressure to diverge, choking with a compressible gas is not possible. Instead, the gas compresses to keep the flow rate below the choking threshold, resulting in a near-choking behavior in which the liquid flow rate closely follows the bubble-position-dependent theoretical threshold regardless of the nominal injection rate of the gas [Fig. 8(a)].

The near-choking regime is similar to phenomena observed in other FSI problems. For example, when a fluid is driven through a confined, deformable porous medium, the imposed pressure gradient squashes the medium against the outlet, which reduces the permeability and ultimately restricts the outflow, i.e., the fluid flux reaches an upper bound and becomes insensitive to further changes of the pressure head [20]. Flow saturation also occurs for inertial flow of a viscous fluid in finite-length elastic tubes: the increasing pressure head reduces the cross-sectional area of the tube leading to

increase in the local fluid velocity, which in turn reduces the internal fluid pressure via the Bernoulli effect and causes further constriction of the tube [40]. Inherently, all of these mechanisms rely on interactions between a flow and an elastic structure, though the details of the FSI are different to the ones considered here.

The study of choking involves the cell gap shrinking to zero. However, our model is formally not valid once the gap becomes too small, as other effects become important, such as adhesion forces between the walls, small-scale roughness of the surfaces, deviations from perfect axisymmetry, and (eventually) the breakdown of the continuum approximation. All of these effects are likely to promote choking by locally enabling initial contact between the walls in isolated azimuthal regions without incurring a divergent pressure. Hence, for example in the near-choking regime, although our model always predicts a very small but nonzero cell gap, in actuality the walls can make contact with each other and choke the flow. This presumably also explains why choking is readily observed in the experiments of Box *et al.* [16] and Peng *et al.* [22].

When the radius of the elastic solid is very large compared with its thickness, long-wave approximations can be applied in the bubble and liquid regions. We have shown that in this regime the elastic cell behaves like a rigid cell, but with modified kinematic and dynamic conditions at the advancing bubble front due to the deformation near the front, and a modified outlet pressure condition due to the bulging near the rim (Sec. V). Although we have assumed axisymmetry in the present study, these approximations readily extend to nonaxisymmetric flows. As a result, the viscous-fingering instability in the elastic-walled cell can be simulated using a standard Hele-Shaw solver for a rigid cell but with modified boundary conditions. Another application for the modified kinematic conditions at the bubble front is to infer the local flux, and hence the global flow rate, from nonaxisymmetric experimental data for the position of the bubble front, as was done by Peng *et al.* [22].

In their experiments performed at larger values of Q_0 , Peng *et al.* [22] suggested that compressibility of the elastic solid will begin to play a role in the problem as the injection pressure approaches a nonnegligible fraction of the bulk modulus of the elastomer. It is straightforward to adapt the present model to account for solid compression, which introduces another nondimensional parameter in the form of Poisson’s ratio ν . However, analysis of the model becomes more difficult, as the long-wave approximation is significantly more complicated [39] and the traveling-wave solutions depend on both ν and the bubble pressure p_b .

The data that support the findings of this study are available on request.

ACKNOWLEDGMENTS

The authors thank F. Box and A. Juel for discussions, and anonymous referees for detailed comments that helped improve the manuscript. The work of the group from Manchester was funded by the EPSRC (Grant No. EP/R045364/1). The work of the group from Oxford was funded by the ERC under the European Union’s Horizon 2020 Programme (Grant No. 805469) and by the EPSRC (Grant No. EP/P009751/1).

APPENDIX: NUMERICAL METHOD

We have implemented a finite-difference scheme in Matlab, making use of its built-in routines for LU factorization and sparse matrix solution. The solid domain $0 \leq r \leq R_{\text{out}}$, $0 \leq z \leq 1$ is discretized using a grid with an initially uniform spacing of 0.02. The radial grid is adapted nonuniformly as required to keep the grid spacing below 2% of the estimated local length scale, and the vertical grid is also refined near the surface to keep the smallest grid cells nearly square.

The solid displacements u_r^s and u_z^s are measured at the midpoint of the horizontal and vertical cell boundaries, respectively, and the solid pressure p^s is measured at the midpoint of each cell. The

associated equations for u_r^s , u_z^s and p^s are

$$\begin{aligned} -\partial_r p^s + \left[\partial_r^2 + \frac{1}{r} \partial_r - \frac{1}{r^2} + \partial_z^2 \right] u_r^s &= 0, & -\partial_z p^s + \left[\partial_r^2 + \frac{1}{r} \partial_r + \partial_z^2 \right] u_z^s &= 0, \\ \left[\partial_r + \frac{1}{r} \right] u_r^s + \partial_z u_z^s &= 0, \end{aligned} \quad (\text{A1})$$

which are evaluated using second-order finite differences. The singularity in the solid equations at $(r, z) = (R, 0)$, due to the discontinuity Δp in the cell pressure p at $r = R$, is treated analytically in a small neighborhood of the bubble front by subtracting a two-dimensional leading-order solution,

$$u_x^s = -\Delta p \frac{z[1 + \ln(x^2 + z^2)]}{4\pi}, \quad u_z^s = -\Delta p \frac{x[1 - \ln(x^2 + z^2)]}{4\pi}, \quad p^s = \Delta p \frac{\pi - 2 \arctan(x/z)}{2\pi}, \quad (\text{A2})$$

where $x = r - R$, which yields additional terms that are proportional to Δp in the equations.

We define an integrated surface displacement ψ , measured on the radial cell boundaries, with the associated equation $\psi = \int_r^{R_{\text{out}}} w r dr$. This allows the equations (6) for the gas and liquid to be written as

$$p = p_b \quad \text{in } r < R, \quad r \partial_r p = -\frac{Q + \dot{\psi}}{b^3} \quad \text{in } R < r < R_{\text{out}}, \quad (\text{A3})$$

which we take to be the equations associated with the variable p .

The time derivative is discretized implicitly as $\dot{\psi} = (\psi - \psi|_{\text{prev}})/\Delta t$, and $\dot{R} = (R - R_{\text{prev}})/\Delta t$, in which $\psi|_{\text{prev}}$ and R_{prev} are the known values from the previous time step, while all other unknowns are to be determined at the current time step. The temporal step size Δt is adapted to keep the relative change in one time step of key quantities such as R and b_{min} around 0.5%. The resulting large nonlinear system of equations is solved using Newton iteration (using the previous values as starting guess), with a decomposition into linear and nonlinear parts to increase efficiency, as follows.

We collect the values of u_r^s , u_z^s , p^s , and ψ in a solution vector \mathbf{X}_L , while the values of p and other individual quantities such as R , \dot{R} , Q , p_b , $b|_{r=R}$, and Δp are collected in \mathbf{X}_N . The complete set of discretized equations to be solved can then be represented as $\mathbf{F}_L(\mathbf{X}_L, \mathbf{X}_N) = \mathbf{0}$ and $\mathbf{F}_N(\mathbf{X}_L, \mathbf{X}_N) = \mathbf{0}$, for the equations associated with \mathbf{X}_L and \mathbf{X}_N , respectively. Given a guess $(\mathbf{X}_L, \mathbf{X}_N)_i$ for the solution vectors, the residuals $\mathbf{F}_{L,N}$ and the Hessian are calculated, and an equation

$$\begin{pmatrix} \mathbf{F}_L \\ \mathbf{F}_N \end{pmatrix} + \begin{pmatrix} A_{LL} & A_{LN} \\ A_{NL} & A_{NN} \end{pmatrix} \left[\begin{pmatrix} \mathbf{X}_L \\ \mathbf{X}_N \end{pmatrix}_{i+1} - \begin{pmatrix} \mathbf{X}_L \\ \mathbf{X}_N \end{pmatrix}_i \right] = \mathbf{0} \quad (\text{A4})$$

for the next iteration is obtained. Here, due to the decomposition into L and N parts, the largest matrix, A_{LL} , is a constant, so its LU factorization can be precomputed and stored (every time the grid is altered), which allows the product of A_{LL}^{-1} with vectors to be calculated efficiently. We then eliminate \mathbf{X}_L from the equations and obtain an expression for \mathbf{X}_N which requires no matrix inversions apart from the precomputed A_{LL}^{-1} and the solution of a matrix equation of approximate size N_r (the number of radial grid points). Although this matrix equation is dense, it is much faster to solve than the original sparse matrix equation of approximate size $3N_r N_z$ (where N_z is the number of vertical grid points).

[1] S. Lee, J. Lee, R. Le Mestre, F. Xu, and C. W. MacMinn, Migration, trapping, and venting of gas in a soft granular material, *Phys. Rev. Fluids* **5**, 084307 (2020).

[2] H. A. Stone, Tuned-in flow control, *Nat. Phys.* **5**, 178 (2009).

- [3] M. Heil and A. L. Hazel, Flow in flexible/collapsible tubes, in *Fluid-Structure Interactions in Low-Reynolds-Number Flows*, edited by C. Duprat and H. A. Stone (Royal Society of Chemistry, London, UK, 2015), pp. 280–312.
- [4] Y. H. Chong, P. H. Gaskell, and N. Kapur, Coating with deformable rolls: An experimental investigation of the ribbing instability, *Chem. Eng. Sci.* **62**, 4138 (2007).
- [5] H. Lin, J. Tan, J. Zhu, S. Lin, Y. Zhao, W. Yu, H. Hojaiji, B. Wang, S. Yang, X. Cheng, Z. Wang, E. Tang, C. Yeung, and S. Emaminejad, A programmable epidermal microfluidic valving system for wearable biofluid management and contextual biomarker analysis, *Nat. Commun.* **11**, 1 (2020).
- [6] T. J. Jones, E. Jambon-Puillet, J. Marthelot, and P.-T. Brun, Bubble casting soft robotics, *Nature* **599**, 229 (2021).
- [7] I. C. Christov, V. Cognet, T. C. Shidhore, and H. A. Stone, Flow rate-pressure drop relation for deformable shallow microfluidic channels, *J. Fluid Mech.* **841**, 267 (2018).
- [8] I. C. Christov, Soft hydraulics: From Newtonian to complex fluid flows through compliant conduits, *J. Phys.: Condens. Matter* **34**, 063001 (2022).
- [9] Q. Yu, J. M. Bauer, J. S. Moore, and D. J. Beebe, Responsive biomimetic hydrogel valve for microfluidics, *Appl. Phys. Lett.* **78**, 2589 (2001).
- [10] A. R. Abate and D. A. Weitz, Single-layer membrane valves for elastomeric microfluidic devices, *Appl. Phys. Lett.* **92**, 243509 (2008).
- [11] C. D. Leslie, C. J. Easley, E. Seker, J. M. Karlinsey, M. Utz, M. R. Begley, and J. P. Landers, Frequency-specific flow control in microfluidic circuits with passive elastomeric features, *Nat. Phys.* **5**, 231 (2009).
- [12] J. Alvarado, J. Comtet, E. d. Langre, and A. E. Hosoi, Nonlinear flow response of soft hair beds, *Nat. Phys.* **13**, 1014 (2017).
- [13] M. Gomez, D. E. Moulton, and D. Vella, Passive Control of Viscous Flow Via Elastic Snap-Through, *Phys. Rev. Lett.* **119**, 144502 (2017).
- [14] X. Wang and I. C. Christov, Theory of the flow-induced deformation of shallow compliant microchannels with thick walls, *Proc. R. Soc. A* **475**, 20190513 (2019).
- [15] A. A. Linninger, M. Xenos, B. Sweetman, S. Ponskshe, X. Guo, and R. Penn, A mathematical model of blood, cerebrospinal fluid and brain dynamics, *J. Math. Biol.* **59**, 729 (2009).
- [16] F. Box, G. G. Peng, D. Pihler-Puzović, and A. Juel, Flow-induced choking of a compliant Hele-Shaw cell, *Proc. Natl. Acad. Sci. USA* **117**, 30228 (2020).
- [17] J. R. Lister, G. G. Peng, and J. A. Neufeld, Viscous Control of Peeling An Elastic Sheet By Bending And pulling, *Phys. Rev. Lett.* **111**, 154501 (2013).
- [18] M. Berhanu, A. Guérin, S. Courrech du Pont, F. Raoult, R. Perrier, and C. Michaut, Uplift of an elastic membrane by a viscous flow, *Phys. Rev. E* **99**, 043102 (2019).
- [19] D. L. Chase, C.-Y. Lai, and H. A. Stone, Relaxation of a fluid-filled blister on a porous substrate, *Phys. Rev. Fluids* **6**, 084101 (2021).
- [20] D. R. Hewitt, J. S. Nijjer, M. G. Worster, and J. A. Neufeld, Flow-induced compaction of a deformable porous medium, *Phys. Rev. E* **93**, 023116 (2016).
- [21] G. Dumazer, B. Sandnes, M. Ayaz, K. J. Måløy, and E. G. Flekkøy, Frictional Fluid Dynamics and Plug Formation in Multiphase Millifluidic Flow, *Phys. Rev. Lett.* **117**, 028002 (2016).
- [22] G. G. Peng, C. Cuttle, F. Box, J. H. Guan, A. Juel, C. W. MacMinn, and D. Pihler-Puzović, Trapping and escape of viscous fingers in a soft Hele-Shaw cell, *Phys. Rev. Fluids* **7**, L062001 (2022).
- [23] P. G. Saffman and G. I. Taylor, The penetration of a fluid into a porous medium or Hele-Shaw cell containing a more viscous liquid, *Proc. R. Soc. A* **245**, 312 (1958).
- [24] D. Pihler-Puzović, P. Illien, M. Heil, and A. Juel, Suppression of Complex Fingerlike Patterns at the Interface Between air and a Viscous Fluid by Elastic Membranes, *Phys. Rev. Lett.* **108**, 074502 (2012).
- [25] A. Juel, D. Pihler-Puzović, and M. Heil, Instabilities in blistering, *Annu. Rev. Fluid Mech.* **50**, 691 (2018).
- [26] D. Pihler-Puzović, G. G. Peng, J. R. Lister, M. Heil, and A. Juel, Viscous fingering in a radial elastic-walled Hele-Shaw cell, *J. Fluid Mech.* **849**, 163 (2018).
- [27] D. Pihler-Puzović, A. Juel, and M. Heil, The interaction between viscous fingering and wrinkling in elastic-walled Hele-Shaw cells, *Phys. Fluids* **26**, 022102 (2014).

- [28] E. B. Arkilic, M. A. Schmidt, and K. S. Breuer, Gaseous slip flow in long microchannels, *J. Microelectromech. Syst.* **6**, 167 (1997).
- [29] G. L. Morini, M. Lorenzini, S. Colin, and S. Geoffroy, Experimental analysis of pressure drop and laminar to turbulent transition for gas flows in smooth microtubes, *Heat Transf. Eng.* **28**, 670 (2007).
- [30] C.-W. Park, S. Gorell, and G. M. Homsy, Two-phase displacement in Hele-Shaw cells: Experiments on viscously driven instabilities, *J. Fluid Mech.* **141**, 275 (1984).
- [31] B. Sandnes, E. G. Flekkøy, H. A. Knudsen, K. J. Måløy, and H. See, Patterns and flow in frictional fluid dynamics, *Nat. Commun.* **2**, 288 (2011).
- [32] C. H. Lee, B. Zhao, R. Abouatallah, R. Wang, and A. Bazylak, Compressible-Gas Invasion Into Liquid-Saturated Porous Media: Application to Polymer-Electrolyte-Membrane Electrolyzers, *Phys. Rev. Appl.* **11**, 054029 (2019).
- [33] C.-Y. Lai, B. Rallabandi, A. Perazzo, Z. Zheng, S. E. Smiddy, and H. A. Stone, Foam-driven fracture, *Proc. Natl. Acad. Sci. USA* **115**, 8082 (2018).
- [34] G. Guyard, F. Restagno, and J. D. McGraw, Elastohydrodynamic Relaxation of Soft and Deformable Microchannels, *Phys. Rev. Lett.* **129**, 204501 (2022).
- [35] C. Cuttle and C. W. MacMinn, Dynamics of Compression-Driven Gas-Liquid Displacement in a Capillary Tube, *Phys. Rev. Lett.* **130**, 114001 (2023).
- [36] C. Cuttle, L. C. Morrow, and C. W. MacMinn, Compression-driven viscous fingering in a radial Hele-Shaw cell, [arXiv:2302.14730](https://arxiv.org/abs/2302.14730).
- [37] B. Sandnes, E. G. Flekkøy, and K. J. Måløy, Stick slip displacement of confined granular mixtures: Bubble expansion, *Eur. Phys. J.: Spec. Top.* **204**, 19 (2012).
- [38] G. G. Peng, D. Pihler-Puzović, A. Juel, M. Heil, and J. R. Lister, Displacement flows under elastic membranes. Part 2. Analysis of interfacial effects, *J. Fluid Mech.* **784**, 512 (2015).
- [39] T. G. J. Chandler, *Mathematical Models of Two-Dimensional Sheets and Foundations*, Ph.D. thesis, University of Oxford, 2021.
- [40] M. Heil and O. E. Jensen, Flow in collapsible tubes and past other highly compliant boundaries, in *Flow in Deformable Tubes and Channels: Theoretical Models and Biological Applications* (Kluwer, Dordrecht, Netherlands, 2003).